

REVERBERATION MAPPING OF PG 0934+013 WITH THE SOUTHERN AFRICAN LARGE TELESCOPE

SONGYOUN PARK¹, JONG-HAK WOO¹, ENCARNI ROMERO-COLMENERO^{2,3}, STEVEN M. CRAWFORD², DAWOO PARK¹, HOJIN CHO¹, YISEUL JEON¹, CHANGSU CHOI¹, AARON J. BARTH⁴, LIUYI PEI⁴, RYAN C. HICKOX⁵, HYUN-IL SUNG⁶, AND MYUNGSHIN IM⁷

¹Department of Physics and Astronomy, Seoul National University, Seoul 08826, Republic of Korea; woo@astro.snu.ac.kr

²South African Astronomical Observatory, P.O. Box 9, Observatory 7935, Cape Town, South Africa

³Southern African Large Telescope Foundation, P.O. Box 9, Observatory 7935, Cape Town, South Africa

⁴Department of Physics and Astronomy, 4129 Frederick Reines Hall, University of California, Irvine, CA 92697-4575, USA

⁵Department of Physics & Astronomy, Dartmouth College, Hanover, NH 03755, USA

⁶Korea Astronomy and Space Science Institute, Daejeon 34055, Republic of Korea

⁷CEOU, Astronomy Program, Department of Physics & Astronomy, Seoul National University, Seoul 08826, Republic of Korea

Draft version October 3, 2017

ABSTRACT

We present the variability and time lag measurements of PG 0934+013 based on a photometric and spectroscopic monitoring campaign over a two year period. We obtained 46 epochs of data from the spectroscopic campaign, which was carried out using the Southern African Large Telescope with ~ 1 week cadence over two sets of 4 month-long observing period, while we obtained 80 epochs of B -band imaging data using a few 1-m class telescopes. Due to the seven month gap between the two observing periods, we separately measured the time lags of broad emission lines including $H\beta$, by comparing the emission line light curve with the B -band continuum light curve using the cross-correlation function techniques. We determined the $H\beta$ lag, $\tau_{\text{cent}} = 8.46_{-2.14}^{+2.08}$ days in the observed-frame based on Year 2 data, while the time lag from Year 1 data was not reliably determined. Using the rms spectrum of Year 2 data, we measured the $H\beta$ line dispersion $\sigma_{\text{line}} = 668 \pm 44 \text{ km s}^{-1}$ after correcting for the spectral resolution. Adopting a virial factor $f = 4.47$ from Woo et al. (2015), we determined the black hole mass $M_{\text{BH}} = 3.13_{-0.93}^{+0.91} \times 10^6 M_{\odot}$ based on the $H\beta$ time lag and velocity.

Keywords: galaxies: active – galaxies: nuclei – galaxies: Seyfert

1. INTRODUCTION

The observed scaling relations between black hole mass (M_{BH}) and the properties of inactive and active galaxies provide interesting constraints in understanding galaxy formation and evolution (see Kormendy & Ho 2013). To investigate the role of BHs in the context of BH-galaxy coevolution (e.g., Peng et al. 2006; Woo et al. 2006; Treu et al. 2007; Jahnke et al. 2009; Merloni et al. 2010; Bennert et al. 2010, 2011; Cisternas et al. 2011; Bennert et al. 2015; Park et al. 2015) as well as the physics of BH accretion and related phenomena (e.g., Woo & Urry 2002; Kollmeier et al. 2006; Davis et al. 2007; Bentz et al. 2013; Woo et al. 2016), BH masses need to be accurately determined.

For active galactic nuclei (AGNs), M_{BH} can be determined with the reverberation mapping technique (Blandford & McKee 1982; Peterson 1993), assuming that the kinematics of the broad-line region (BLR) gas are governed by the gravitational potential of the central BH. The presence of broad emission lines and flux variability, as one of the main characteristics of type 1 AGNs, allows us to probe the geometry, structure, and kinematics of BLR. The light-travel time to the BLR can be determined by measuring the time delay of variations between continuum and emission lines, which is then translated to the BLR size. The measured BLR size using $H\beta$ emission line and AGN continuum luminosity at 5100Å has been reported in the literature, ranging from a few light days to a couple of hundred light days in the rest-frame (e.g., Bentz et al. 2013). As a measure of the gas

velocity, either the second moment (line dispersion; σ_{line}) or the full-width half maximum (FWHM) of the broad emission line profile is typically adopted from the mean or rms spectra generated based on multi-epoch data (see e.g., Peterson et al. 2004; Park et al. 2012). Combining the time lag and the width of broad emission lines, mass can be determined as $M_{\text{BH}} \propto R_{\text{BLR}} V^2$, where R_{BLR} is the measured time lag between AGN continuum and the BLR, while V is velocity measured from the width of the broad-emission line (Peterson 1993).

Reverberation mapping data are of paramount importance since they provide the fundamental calibration for indirect M_{BH} estimators. Consequently, M_{BH} of distant type 1 AGNs can be estimated based on a single-epoch spectrum, instead of a directly measured time lag from a long-term monitoring campaign (Kaspi et al. 2000; Vestergaard & Peterson 2006; McGill et al. 2008; Woo et al. 2015; Park et al. 2017). In this method AGN continuum luminosities are used as a proxy for R_{BLR} based on the empirical size-luminosity relation between the measured R_{BLR} and AGN luminosity at 5100 Å (e.g., Bentz et al. 2013). However, these indirect mass estimates are much more uncertain than reverberation masses (a factor of 2-3 in the case of $H\beta$ -based mass estimates; Woo et al. 2010; Park et al. 2012) and mainly rely on the limited calibration based on the relatively small sample of reverberation-mapped AGNs (e.g., Woo et al. 2013; Grier et al. 2013; Woo et al. 2015). Thus, enlarging the reverberation-mapped AGNs can provide better calibration and reduce the systematic uncertainties in the

single-epoch mass estimators.

The reverberation mapping technique has been successfully applied to several dozens of AGNs to date (e.g., Wandel et al. 1999; Kaspi et al. 2000; Peterson et al. 2004; Bentz et al. 2009a; Barth et al. 2011; Grier et al. 2013; Barth et al. 2015; Fausnaugh et al. 2017). Various reverberation projects, including campaigns utilizing multi-object spectrographs or robotic monitoring, are currently devised or underway (e.g. Valenti et al. 2015; Shen et al. 2015). One of the difficulties of the reverberation mapping is that a long-term spectroscopic monitoring with relatively short cadence is required to obtain accurate time lag measurements. So far, most reverberation studies have been performed with relatively small telescopes while it would be more efficient with larger-aperture and service mode telescopes (e.g., see a recent reverberation study with the HET by Rafter et al. 2011).

As a pilot study with the Southern African Large Telescope (SALT), which provides the unique capability of quasi-daily access, efficient service observations, and large photon-collecting power, we performed a reverberation mapping campaign of a nearby Seyfert 1 galaxy PG 0934+013 at R.A. = 09:37:1.0, Dec. = +01:05:43, and redshift $z = 0.0503$ (Véron-Cetty et al. 2001). The target is also known as Mrk 707, which was classified as a narrow-line Seyfert 1 galaxy since the FWHM of the $H\beta$ line was reported to be less than 2000 km s^{-1} (e.g., 1320 km s^{-1} by Boroson & Green 1992). The host galaxy is a spiral galaxy with clear signs of spiral arms and a bar structure (see S 4.2). We selected this target among bright AGNs from the Palomar Bright Quasar Survey (Schmidt & Green 1983), that are observable at the SALT at least over 4 months per year. In this paper, we present the results from our reverberation mapping campaign, which was carried out over two seasons, using the SALT for spectroscopy and three smaller telescopes for photometry.

2. OBSERVATIONS AND DATA REDUCTION

2.1. Photometry

We carried out imaging observations for the broad band photometry, using the B -band filter. In total we obtained B -band photometry from 80 epochs during the campaign. We started the photometry campaign on December 6th 2016 with a ~ 4 day cadence, using the Faulkes Telescope North (FTN) 2-m in Hawaii, which is one of the Las Cumbres Observatory Global Telescopes (LCOGT). The campaign lasted until April 11th 2013 when the target became unobservable. We will call this campaign period as Year 1. Additionally, we obtained 3 epochs in October 2012. In the second year we continued the campaign from December 10th 2013 to May 12th 2014 with a ~ 5 day cadence (Year 2), using the Mt. Lemon Optical Astronomy Observatory (LOAO) 1-m telescope in Arizona. During the second year campaign, we also used the Faulkes Telescope South (FTS) for seven epochs between December 2013 and January 2014 to assist the LOAO campaign. However, we mainly used the LOAO data for the reverberation analysis for Year 2.

Both LCOGT 2-m telescopes (FTN and FTS) have the same detector: $4K \times 4K$ Fairchild CCD with a $15\mu\text{m}$ pixel size, providing a $10' \times 10'$ field of view (FoV). The images

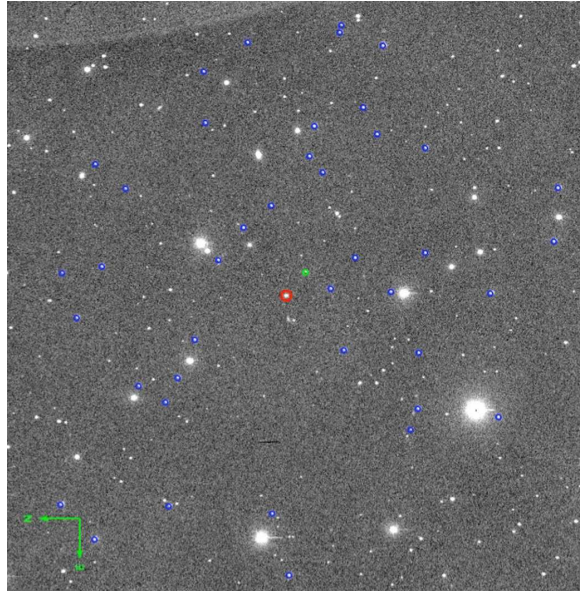


Figure 1. B-band image of PG 0934+013 (green circle) obtained at the LOAO 1-m telescope. Comparison stars, which were used in the differential photometry, are denoted with blue circles while the comparison star in the slit for the SALT spectroscopy is marked with a red circle. The FoV is $28' \times 28'$.

were taken in 2×2 pixel binning mode with a spatial scale of $0''.304 \text{ pixel}^{-1}$. LOAO 1-m telescope has a $4K \times 4K$ E2V CCD detector with a $15\mu\text{m}$ pixel size, providing a $28' \times 28'$ FoV. We used 2×2 pixel binning mode, which corresponds to a pixel scale of $0''.796 \text{ pixel}^{-1}$.

We determined the exposure time for B -band photometry to obtain high quality data. Typical total exposure time was 180 and 480 seconds, respectively for FT and LOAO, which is divided into 3 to 4 exposures. The quality of images is good enough for differential photometry except for a couple of epochs when the sky condition was bad (e.g., seeing, cirrus, etc).

FT data were delivered to us after pre-process (i.e., bias subtraction and flat fielding), while for the LOAO data, we preprocessed the data following the standard IRAF procedure. We combined individual exposures using median combine for each night, generating one image per epoch. Cosmic-rays were removed with the LA-Cosmic task (van Dokkum 2001). Photometric measurements for the target AGN and comparison stars in the field were carried out using SExtractor (Bertin & Arnouts 1996). We performed aperture photometry using various aperture sizes ranging from $1''$ to $20''$ diameters, to test the seeing effect and the reliability of the flux measurements. We found that the aperture diameter of $7''$ provides an optimal aperture with a minimum systematic variation. Thus, we used a $7''$ aperture for all sources in the FoV.

Since our goal is to perform differential photometry for measuring the relative flux change, we used a num-

ber of stars in the FoV to calculate zero-points of each epoch assuming these stars are not variable. For this step, we selected bright stars, which have the uncertainty of the instrumental magnitude less than 1%. All of these stars turn out to have $B < 17$ mag. Typically ~ 10 and ~ 40 stars were used as comparison stars, respectively for LCOGT and LOAO data (see Figure 1).

We chose the best epoch when the sky condition was close to photometric and calculated the magnitude difference ($\Delta\text{mag.}$) of each star between the standard epoch and each epoch. The average of $\Delta\text{mag.}$ provides the zero point of given epochs while the standard deviation of $\Delta\text{mag.}$ represents the systematic uncertainty of the zero points, which is typically 0.03 mag for LCOGT and 0.02 mag for LOAO photometry. Once we obtained the zero point for each epoch using the $\Delta\text{mag.}$ method, we rescaled all magnitude measurements using the zero point. As a consistency check, we calculated the rms variability of each comparison star, and found that flux variability is less than 0.02-0.03 mag during the campaign, suggesting that the $\Delta\text{mag.}$ method provided reliable calibration within a few percent systematic uncertainty. At the same time, we confirmed that these comparison stars were not variable based on the results from the differential photometry.

As a standard star, we used a bright star ID 0910-0183676 (R.A.=09:36:59.60, Dec.=+01:03:40.5), which is close to the target AGN, and adopted the B -band magnitude $B_1=15.72$ from USNO B1.0 catalog. Assuming that B magnitude of LCOGT and LOAO are similar to B_1 magnitude of USNO B1.0 catalog, we then calibrated all magnitude measurements. Since our aim is to measure the time lag between photometry and spectroscopy, this simple calibration is acceptable without affecting the time-lag measurements. Table 1 lists the calibrated B -band magnitude of PG 0934+013. The quoted uncertainty was derived by combining the measurement error (i.e., standard photometric error) from SExtractor and the systematic error based on the rms scatter of the zero point of individual comparison stars.

2.2. Spectroscopy

Spectroscopic observations were performed during 46 nights scheduled between December 20th 2012 and April 29th 2014, along with a seven month gap between Year 1 and Year 2 due to the lack of observability. Spectroscopic observations were carried out with the Robert Stobie Spectrograph (e.g., Burgh et al. 2003; Kobulnicky et al. 2003) at the SALT (Buckley et al. 2006), which was entirely performed in service mode. The B -band magnitude of the target was reported as 16.3 by Schmidt & Green (1983) and we calculated the $H\beta$ lag based on the monochromatic luminosity at 5100\AA measured from the observed flux in the SDSS spectrum, using the size-luminosity relation from Bentz et al. (2013). The expected lag is ~ 25 days although its value has large uncertainty due to the variability and the contribution from the host galaxy emission to the observed continuum flux. Assuming that the actual lag would be close to 25 days, we chose a \sim five day cadence for the monitoring program, to obtain sufficient time resolution for cross correlation analysis.

We used a spectral setup with the PG2300 grating cen-

tered at 5136\AA , covering a spectral range between 4636\AA and 5636\AA , in which the $H\beta$ and [O III] emission lines are located between the two gaps in the CCD. To minimize the slit loss we used slit width $4''$. The spectral resolution is $R = 1040$ at the center of the spectral range while the spatial scale is $0''.254\text{ pixel}^{-1}$ in the 2×2 binning mode. We used the position angle from North to East 50.5° to include a comparison star in the slit for experimenting flux calibration. However, we did not attempt to perform flux calibration based on the comparison star in the slit since the SALT flux calibration has large uncertainty due to the vignetting, which changes at each epoch. During the first 5 epochs in Year 1, the spectral set-up was not optimal, hence we adjusted the grating angle to move a part of blue wing of $H\beta$ emission line out of the CCD gap in the spectral range. Also, we increased the slit width from $2''$ to $4''$ for the rest of the campaign. Note that these 5 epochs were not included in the analysis.

We determined the exposure time using the RSS simulator¹ to achieve high $S/N > 20$. We initially used a total of 360 second exposure per epoch, then increased the exposure time to 540 second, which was divided into 2 readouts (see Table 3). Arc lamp and dome flat images were taken each night for standard calibration. Spectroscopic data were processed by the SALT PyRAF package (PySALT; Crawford et al. 2010), which includes bias subtraction, flat-fielding, gain correction, cross-talk correction, and amplifier mosaicking. Cosmic rays were cleaned using the LA-Cosmic routine (van Dokkum 2001). Wavelength calibration was performed by identifying the arc lines from arc spectra and rectifying spectral image based on a polynomial fit. The spectral images were combined using a median combine. Then, we extracted one dimensional spectra with a $7.62''$ aperture size, using the procedures in the PySALT package. The median S/N per pixel at 5100\AA is ~ 37 (see Table 2).

Flux calibration was initially performed using spectrophotometric standard stars, which were observed during 11 nights out of the total 46 nights. Note that standard stars are typically observed on a weekly basis at the SALT to constrain the response function over the spectral range. For the nights when standard stars were not observed, we adopted the flux calibration from adjacent observing dates as we assumed the response function would be similar for a given small spectral range (i.e., including $H\beta$ and [O III]). Since the uncertainty of the flux calibration of the SALT spectroscopy is relatively large, we recalibrated each spectrum based on the narrow emission line [OIII] $\lambda 5007$, which is expected to be non-variable in the time scale of our observing campaign. For this process, we followed the procedure outlined by van Groningen & Wanders (1992), by shifting and rescaling individual spectra with respect to the reference spectrum, which was averaged from all spectra obtained during the campaign. We first decomposed each spectrum as described in the next Section and measured the flux of the [O III] line using the best-fit model. Then, we rescaled each spectrum to match the [O III] flux.

In addition, we also used the flux calibration code

¹ <http://astronomers.salt.ac.za/software/rss-simulator/>

presented by Fausnaugh (2017), who used the same scheme of van Groningen & Wanders (1992). The code by Fausnaugh (2017) is less dependent on the spectral resolution, which may vary night-to-night due to the varying seeing, and provides a better smoothing kernel with Gauss-Hermite polynomials for matching the spectral resolution. The code uses a Bayesian formalism for fitting the line profiles and estimating parameter uncertainties. As a consistency check of the flux recalibration, we employed this code to rescale individual spectra and obtained the $H\beta$ light curve and the $H\beta$ lag, which were consistent with the measurements based on our own rescaling method (see more details in Section 3.2).

3. ANALYSIS

3.1. Multi-component Fitting

We performed multi-component spectral fitting to measure the fluxes and widths of the major emission lines, e.g., $H\beta$, [O III], and He II. Each spectrum was decomposed into AGN featureless continuum, the Fe II emission blends, $H\beta$, [O III], and He II emission lines (see Woo et al. 2006; Park et al. 2012). The Levenberg-Marquardt routines in the IDL `mpfit` package (Markwardt 2009) were adopted to determine the best model based on χ^2 minimization. We used a power-law component to represent featureless AGN continuum while the stellar component becomes negligible in the fitting process in most cases except for several epochs with high S/N (i.e., $> \sim 50$) when stellar absorption lines were noticeable. Generally, stellar lines were very weak although we see the sign of stellar absorption lines (i.e., Mgb triplet and Fe 5270 Å) in the residual (see Figure 2).

Fe II emission blends were initially modeled with the Fe II template from Boroson & Green (1992). However, due to the strong Fe II emission features between $H\beta$ and [O III] $\lambda 4696$, and redward of [O III] $\lambda 5007$, this template failed to provide acceptable fitting results. Instead, we used the Fe II template provided by Kovačević et al. (2010), who divided the Fe II complex into five groups, so that various flux ratios among these five groups can be applied. We find that this template provides better fit although the strong Fe II emission features between $H\beta$ and [O III] $\lambda 4696$ cannot be subtracted entirely. Since we mainly focus on the $H\beta$ line flux measurements, we accept these results for our variability analysis. In the case of the He II line, we modeled the line profile with broad and narrow components using two Gaussian components, which provided successful results. For the $H\beta$ $\lambda 4861$ and [O III] $\lambda\lambda 4959, 5007$ lines, we used a more complex fit. A tenth-order Gauss-Hermite series (van der Marel 1994) was employed to fit [O III] $\lambda 5007$ in the range of 4979–5022 Å. The [O III] $\lambda 4959$ line was modeled with the same velocity profile and the flux scale of 1/3. The $H\beta$ narrow component was also constructed using the [O III] profile after scaling to match the $H\beta$ narrow component. A typical flux scale between narrow $H\beta$ and [O III] $\lambda 5007$ is 0.19. Finally, the $H\beta$ broad component was modeled using a tenth-order Gauss-Hermite functions in the range of 4791–4931 Å. We fit all aforementioned components simultaneously and measured the line fluxes based on the best model (cf. Woo et al. 2006; Park et al. 2012; Barth et al. 2015). In Figure 2, we present an example of the best-fit model. Note that since it is difficult to sep-

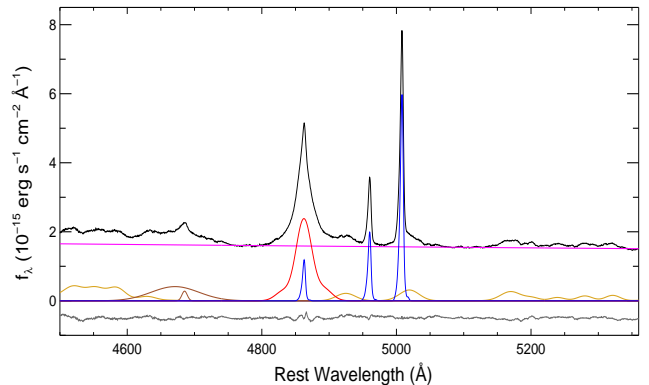


Figure 2. Example of the spectral decomposition with multi-components. The mean spectrum (black) is modeled with a power-law continuum (magenta), a broad component of $H\beta$ (red), a narrow component of $H\beta$ (blue), [O III] $\lambda\lambda 4959, 5007$ (blue), broad and narrow components of He II (brown), and Fe II emission blends (yellow). At the bottom, the residual of the fit is presented with a grey line.

arate the narrow and broad components in the $H\beta$ line profile as the flux ratio between $H\beta$ and [O III] changes epoch to epoch in the fitting process, we decided to use the total flux of the $H\beta$ line profile for time lag analysis, in order to avoid additional systematic uncertainties. Thus, the variability of $H\beta$ is slightly underestimated since the constant narrow $H\beta$ flux is added.

3.2. Time Lag Measurements

In Figure 3 we present the light curves of B -band photometry, $H\beta$, He II emission lines, and Fe II emission blends. The B -band magnitude measurements are listed in Table 1 while the spectroscopic flux measurements of each emission line are listed in Table 2. We quantified the variability of each light curve using F_{var} , which is defined as

$$F_{\text{var}} = \frac{\sqrt{\sigma^2 - \langle \delta^2 \rangle}}{\langle f \rangle} \quad (1)$$

where σ^2 is the variance of the fluxes, $\langle \delta^2 \rangle$ is the rms uncertainty, and $\langle f \rangle$ is the mean of the observed fluxes (Rodríguez-Pascual et al. 1997; Edelson et al. 2002). We find that F_{var} is larger than 0.1 for all light curves, indicating high variability as listed in Table 3. The He II emission line shows the highest variability amplitude, which is roughly two times higher than those of $H\beta$ and Fe II. We also calculated R_{max} , which is the ratio of the maximum and minimum fluxes in the light curve, finding that the fluxes of the continuum and $H\beta$ and Fe II have increased by 50–60% during the campaign, while He II shows more than a factor of 2 increase.

Using the light curves presented in Figure 3, we calculated the cross correlation function (CCF) to measure the time lag between continuum and each emission line, following the procedure described by Peterson et al. (2004). Due to the seven month gap between two monitoring campaigns, we separately determined a CCF for each year. Since the continuum and emission line data were unevenly sampled, we first re-distributed the data by interpolating B -band light curve with respect to the emission line sampling, then derived the correlation coefficient. In the same way, we interpolated the light curve of each emission line with respect to continuum

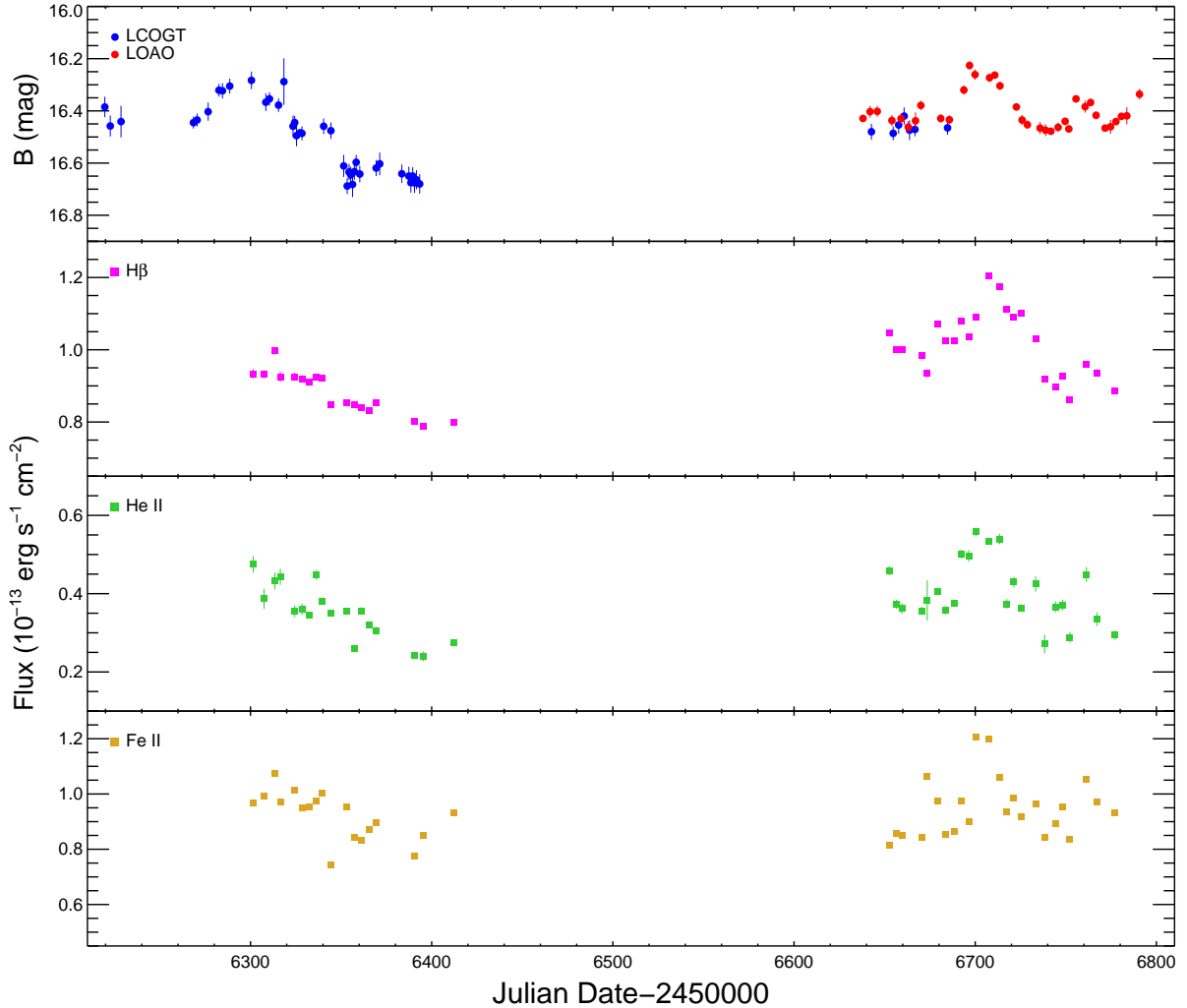


Figure 3. Light curves of the B band, the $H\beta$, He II, and Fe II emission lines (from top to bottom).

sampling, then calculated the CCF (Gaskell & Peterson 1987; White & Peterson 1994; Peterson et al. 2004). The CCF was computed for time lags ranging from -20 to 60 days with increments of 0.25 days. Once we obtained two CCF results, we used the averaged CCF for determining the time lags and their uncertainties. We determined time lags using two different definitions: τ_{peak} using the peak of CCF, and τ_{cen} using the centroid of CCF, which was calculated using the points with $\text{CCF} \geq 0.8 \times \text{CCF}_{\text{peak}}$.

The final time lags and their uncertainties were determined by using Monte Carlo realization ($N=10,000$) based on flux randomization and random subset sampling (FR/RSS) method (Gaskell & Peterson 1987; White & Peterson 1994; Peterson et al. 2004). We randomly selected the same number of data points from the light curve, allowing duplication. If one epoch was selected m times, then we decreased the uncertainty of the flux by $m^{1/2}$. Using the selected epoch, then we simulated mock light curves by adding Gaussian random noise based on the flux errors at each epoch, and computed the CCF of the generated continuum and emission light curves. From the distribution of the lag measurements, we adopted the mean value as the final time lag, and

the difference between the mean and the highest (lowest) 1σ value in the distribution of CCF was adopted for uncertainty.

Figure 4 presents the results of CCF calculation between the continuum and the $H\beta$ emission line. We measured the time lag $\tau_{\text{peak}} = 8.52^{+2.23}_{-2.27}$ days, and $\tau_{\text{cen}} = 8.46^{+2.08}_{-2.14}$ days in the observed frame from Year 2 data while we were not able to determine the time lag based on Year 1 data due to the monotonic decrease of the $H\beta$ flux. For a consistency check for the interpolation process and cross correlation analysis, we used the JAVELIN code (Zu et al. 2013) to perform CCF calculation based on Year 2 data, obtaining $H\beta$ time lag $\tau_{\text{JAVELIN}} = 8.32 \pm 2.04$ days in the observed frame, which is consistent within the uncertainty.

Considering the uncertainties due to the flux recalibration based on [O III], we also tested how the lag measurement changes if we use the rescaled spectra using the code by Fausnaugh (2017). We found that when we decomposed each spectrum and used the emission line spectrum for flux rescaling after subtracting FeII complex and the power-law component, we obtained a very similar $H\beta$ light curve except for a few epochs, which showed the lowest S/N among all epochs. Based on the

Table 1
B-band Magnitude

| Year 1 (2012-2013) | | Year 2 (2013-2014) | |
|-----------------------|--------------|-----------------------|--------------|
| JD | <i>B</i> | JD | <i>B</i> |
| (days) | (mag) | (days) | (mag) |
| (1) | (2) | (3) | (4) |
| 6219.586 ^a | 16.39 ± 0.04 | 6638.050 | 16.43 ± 0.01 |
| 6222.612 ^a | 16.46 ± 0.04 | 6641.947 | 16.40 ± 0.02 |
| 6228.556 ^a | 16.44 ± 0.06 | 6642.717 ^b | 16.48 ± 0.03 |
| 6268.528 | 16.45 ± 0.02 | 6645.930 | 16.40 ± 0.02 |
| 6270.530 | 16.43 ± 0.02 | 6654.017 | 16.44 ± 0.02 |
| 6276.618 | 16.40 ± 0.03 | 6654.719 ^b | 16.49 ± 0.03 |
| 6282.601 | 16.32 ± 0.02 | 6657.722 ^b | 16.45 ± 0.03 |
| 6284.527 | 16.32 ± 0.03 | 6659.052 | 16.43 ± 0.02 |
| 6288.545 | 16.30 ± 0.03 | 6660.753 ^b | 16.42 ± 0.03 |
| 6300.529 | 16.28 ± 0.03 | 6663.034 | 16.46 ± 0.02 |
| 6308.450 | 16.37 ± 0.03 | 6663.750 ^b | 16.47 ± 0.04 |
| 6310.464 | 16.35 ± 0.03 | 6666.734 ^b | 16.47 ± 0.03 |
| 6315.473 | 16.38 ± 0.03 | 6667.051 | 16.44 ± 0.03 |
| 6318.445 | 16.29 ± 0.09 | 6669.991 | 16.38 ± 0.02 |
| 6323.469 | 16.46 ± 0.04 | 6680.954 | 16.43 ± 0.02 |
| 6324.400 | 16.45 ± 0.03 | 6684.711 ^b | 16.46 ± 0.03 |
| 6325.400 | 16.50 ± 0.04 | 6685.719 | 16.43 ± 0.02 |
| 6327.379 | 16.48 ± 0.01 | 6693.718 | 16.32 ± 0.02 |
| 6328.401 | 16.49 ± 0.03 | 6696.858 | 16.23 ± 0.02 |
| 6340.386 | 16.46 ± 0.03 | 6699.896 | 16.26 ± 0.02 |
| 6344.383 | 16.48 ± 0.03 | 6707.892 | 16.27 ± 0.02 |
| 6351.457 | 16.61 ± 0.04 | 6710.767 | 16.26 ± 0.01 |
| 6353.379 | 16.69 ± 0.03 | 6713.646 | 16.30 ± 0.02 |
| 6354.383 | 16.63 ± 0.03 | 6722.716 | 16.39 ± 0.01 |
| 6355.296 | 16.64 ± 0.03 | 6725.855 | 16.43 ± 0.02 |
| 6356.315 | 16.68 ± 0.05 | 6728.776 | 16.45 ± 0.02 |
| 6357.335 | 16.63 ± 0.03 | 6735.794 | 16.47 ± 0.02 |
| 6358.336 | 16.60 ± 0.03 | 6738.806 | 16.47 ± 0.02 |
| 6360.320 | 16.64 ± 0.03 | 6741.732 | 16.48 ± 0.01 |
| 6369.366 | 16.62 ± 0.03 | 6745.740 | 16.46 ± 0.02 |
| 6371.333 | 16.60 ± 0.04 | 6749.612 | 16.44 ± 0.01 |
| 6383.522 | 16.64 ± 0.04 | 6751.653 | 16.47 ± 0.01 |
| 6387.403 | 16.65 ± 0.04 | 6755.625 | 16.35 ± 0.01 |
| 6388.536 | 16.68 ± 0.04 | 6760.658 | 16.38 ± 0.02 |
| 6389.536 | 16.65 ± 0.03 | 6763.648 | 16.37 ± 0.01 |
| 6390.528 | 16.68 ± 0.04 | 6766.699 | 16.42 ± 0.01 |
| 6391.572 | 16.66 ± 0.04 | 6771.667 | 16.47 ± 0.01 |
| 6393.377 | 16.68 ± 0.04 | 6774.686 | 16.46 ± 0.03 |
| | | 6777.653 | 16.44 ± 0.01 |
| | | 6780.670 | 16.42 ± 0.01 |
| | | 6783.659 | 16.42 ± 0.03 |
| | | 6790.655 | 16.34 ± 0.02 |

Note. — Col. 1: Julian date (-2,450,000). Col. 2: *B*-band magnitude in Year 1. Col. 3: Julian date (-2,450,000). Col. 4: *B*-band magnitude in Year 2.

^a These epochs were not used for the CCF analysis because of a large time gap.

^b The data of these epochs were obtained at the FTS in Year 2, and excluded for the CCF analysis.

Monte Carlo simulations, we obtained the $H\beta$ time lag $\tau_{\text{cen}} = 8.84_{-2.35}^{+2.26}$ days, which is consistent with the results based on our own flux rescaling method within the uncertainties. Thus, we confirm that the difference of the flux rescaling method is insignificant for time lag measurements. In contrast, when we used the original spectra without subtracting FeII complex and the power-law component, we obtained a very different light curve and failed to obtain a reliable lag measurement. We suspect that these results are due to the fact that the Fe II feature, that is blended with [O III] $\lambda 5007$, is very strong and its variability may cause systematic uncertainties in measuring [O III] flux in each single-epoch spectrum if the decomposition is not properly performed.

We also investigated the time lag of the He II line and Fe II blends (see Table 4). While the distribution of the CCF of He II was not well-constrained with Year 1 data,

Table 2
Emission line fluxes

| JD | t_{exp} | S/N | $f_{H\beta}$ | f_{HeII} | f_{FeII} |
|----------|------------------|-----|---|-------------------|-------------------|
| (days) | (s) | | (10^{-15} erg s $^{-1}$ cm $^{-2}$) | | |
| (1) | (2) | (3) | (4) | (5) | (6) |
| 6301.511 | 360 | 28 | 93.36 ± 1.27 | 47.49 ± 2.10 | 96.92 ± 0.27 |
| 6307.492 | 360 | 41 | 93.23 ± 1.12 | 38.67 ± 2.59 | 99.34 ± 0.29 |
| 6313.475 | 360 | 45 | 99.66 ± 0.96 | 43.24 ± 2.16 | 107.46 ± 0.28 |
| 6316.448 | 360 | 29 | 92.52 ± 1.37 | 44.32 ± 2.06 | 97.05 ± 0.34 |
| 6324.417 | 540 | 30 | 92.54 ± 1.14 | 35.51 ± 1.47 | 101.44 ± 0.19 |
| 6328.446 | 540 | 52 | 92.01 ± 0.98 | 36.01 ± 1.47 | 94.97 ± 0.21 |
| 6332.388 | 540 | 55 | 91.17 ± 0.53 | 34.52 ± 0.74 | 95.47 ± 0.13 |
| 6336.392 | 540 | 62 | 92.34 ± 0.53 | 44.79 ± 1.31 | 97.55 ± 0.13 |
| 6339.444 | 540 | 66 | 92.15 ± 0.49 | 38.16 ± 0.86 | 100.36 ± 0.12 |
| 6344.352 | 540 | 23 | 84.79 ± 0.36 | 35.14 ± 0.56 | 74.33 ± 0.09 |
| 6353.339 | 540 | 29 | 85.23 ± 0.44 | 35.53 ± 0.83 | 95.32 ± 0.11 |
| 6357.323 | 540 | 43 | 84.82 ± 0.35 | 26.04 ± 0.65 | 84.32 ± 0.11 |
| 6361.360 | 540 | 41 | 83.92 ± 0.47 | 35.64 ± 0.87 | 83.15 ± 0.11 |
| 6365.350 | 540 | 53 | 83.19 ± 0.39 | 31.97 ± 0.84 | 87.30 ± 0.12 |
| 6379.380 | 540 | 18 | 85.33 ± 0.44 | 30.51 ± 0.99 | 89.63 ± 0.14 |
| 6390.296 | 540 | 46 | 80.13 ± 0.35 | 24.32 ± 0.76 | 77.48 ± 0.10 |
| 6395.304 | 540 | 32 | 78.86 ± 0.41 | 23.98 ± 1.26 | 84.95 ± 0.12 |
| 6412.254 | 540 | 51 | 79.80 ± 0.40 | 27.47 ± 0.87 | 93.28 ± 0.12 |
| 6652.544 | 540 | 28 | 104.56 ± 0.66 | 45.87 ± 1.12 | 81.29 ± 0.15 |
| 6656.532 | 540 | 49 | 99.97 ± 0.61 | 37.30 ± 1.14 | 85.58 ± 0.19 |
| 6659.514 | 540 | 46 | 100.06 ± 0.76 | 36.22 ± 1.34 | 84.96 ± 0.15 |
| 6670.473 | 720 | 27 | 98.31 ± 0.89 | 35.62 ± 1.06 | 84.40 ± 0.16 |
| 6673.509 | 540 | 20 | 93.45 ± 1.04 | 38.29 ± 5.12 | 106.41 ± 0.15 |
| 6679.462 | 1080 | 41 | 107.15 ± 0.47 | 40.56 ± 0.93 | 97.52 ± 0.11 |
| 6683.471 | 540 | 39 | 102.51 ± 0.57 | 35.75 ± 1.09 | 85.30 ± 0.16 |
| 6688.420 | 540 | 33 | 102.37 ± 0.59 | 37.56 ± 0.91 | 86.60 ± 0.15 |
| 6692.489 | 540 | 39 | 107.88 ± 0.60 | 50.11 ± 1.12 | 97.35 ± 0.13 |
| 6696.406 | 540 | 44 | 103.60 ± 0.75 | 49.66 ± 1.46 | 89.93 ± 0.14 |
| 6700.379 | 540 | 23 | 108.92 ± 0.64 | 55.76 ± 1.06 | 120.54 ± 0.17 |
| 6707.408 | 540 | 22 | 120.33 ± 0.45 | 53.41 ± 0.85 | 119.73 ± 0.11 |
| 6713.476 | 540 | 44 | 117.51 ± 0.74 | 53.98 ± 1.31 | 105.95 ± 0.18 |
| 6717.349 | 540 | 40 | 111.25 ± 0.65 | 37.39 ± 1.20 | 93.64 ± 0.17 |
| 6721.338 | 540 | 43 | 109.14 ± 0.77 | 42.95 ± 1.34 | 98.48 ± 0.16 |
| 6725.318 | 540 | 23 | 110.08 ± 0.61 | 36.35 ± 0.93 | 91.90 ± 0.17 |
| 6733.303 | 540 | 13 | 103.12 ± 0.54 | 42.48 ± 1.93 | 96.41 ± 0.16 |
| 6738.301 | 540 | 43 | 91.99 ± 0.83 | 27.16 ± 2.36 | 84.31 ± 0.23 |
| 6744.297 | 540 | 43 | 89.61 ± 0.76 | 36.65 ± 1.39 | 89.33 ± 0.18 |
| 6748.266 | 540 | 31 | 92.60 ± 0.62 | 37.10 ± 1.37 | 95.36 ± 0.17 |
| 6752.270 | 540 | 37 | 86.17 ± 0.74 | 28.85 ± 1.32 | 83.60 ± 0.25 |
| 6761.359 | 540 | 15 | 95.85 ± 0.83 | 44.90 ± 1.90 | 105.22 ± 0.13 |
| 6767.261 | 540 | 46 | 93.58 ± 1.05 | 33.51 ± 1.72 | 97.11 ± 0.18 |
| 6777.244 | 540 | 33 | 88.52 ± 0.66 | 29.40 ± 1.17 | 93.31 ± 0.16 |

Note. — Col. 1: Julian date (-2,450,000). Col. 2: Exposure time. Col. 3: Signal-to-noise per pixel averaged in the range of 5090-5110 Å. Col. 4: Flux of $H\beta$ emission line. Col. 5: Flux of He II emission line. Col. 6: Flux of Fe II emission blends.

Table 3
Variability of continuum and emission lines

| | F_{var} | R_{max} |
|----------------|------------------|------------------|
| <i>B</i> -band | 0.11 | 1.53 ± 0.05 |
| $H\beta$ | 0.11 | 1.53 ± 0.01 |
| He II | 0.22 | 2.33 ± 0.13 |
| Fe II | 0.10 | 1.62 ± 0.01 |

we were able to measure the time lags of He II for Year 2 (Figure 5). These results are expected in Figure 3 as the light curve of He II in Year 1 shows monotonic decrease without a strong bump. We determined the time lag of He II in the observed frame as $\tau_{\text{peak}} = 0.92_{-2.42}^{+1.58}$ days and $\tau_{\text{cen}} = 0.84_{-2.19}^{+2.05}$ days based on Year 2 data. Although the measured He II lag is consistent with zero within the uncertainty, it suggests that the He II lag is much shorter than the $H\beta$ lag. This result is consistent with the fact that He II is strongly variable and promptly responding to continuum emission as also noted by previous reverberation mapping results (Peterson & Ferland 1986;

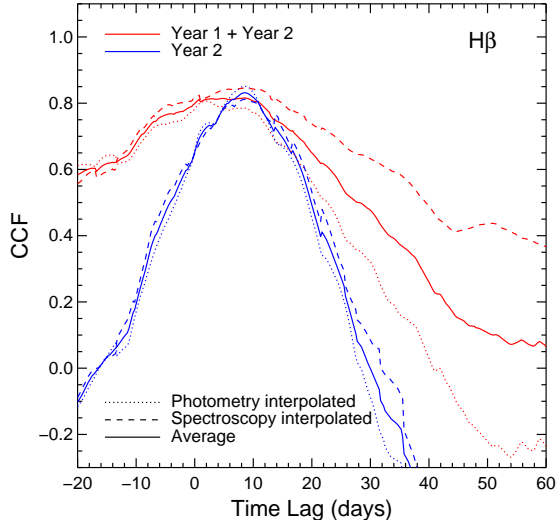


Figure 4. Cross-correlation function between the B -band continuum and $H\beta$ emission line, respectively for Year 1 + Year 2 (red) and year 2 (blue). CCF values are calculated by interpolating photometry data (dotted) or spectroscopy data (dashed) data, respectively. The average of the two CCF results are denoted with solid lines.

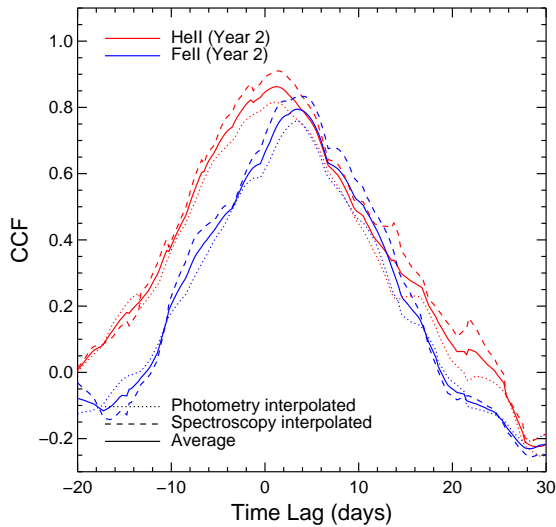


Figure 5. Cross-correlation function between the B -band continuum and He II emission line (red) and Fe II emission blends (blue) based on Year 2 data.

Kollatschny 2003; Pei et al. 2014; Barth et al. 2015).

For Fe II, the light curve in Year 1 appears to have a similar trend to $H\beta$, but the CCF was not well-defined. Instead, we determined the Fe II lag $\tau_{\text{peak}} = 3.51^{+1.49}_{-2.76}$ days and $\tau_{\text{cen}} = 3.74^{+1.97}_{-2.62}$ days in the observed frame based on Year 2 data. This result suggests that Fe II emission appears to be located in an inner region than $H\beta$ (cf. Barth et al. 2013; Hu et al. 2015). However, due to the large uncertainty of the lag and the relatively weak CCF result (see Fig. 4), further analysis based on a better quality light curve is needed to derive more reliable conclusion.

3.3. Line Width Measurements

Table 4
Time lag measurements in the observed-frame

| | | τ_{peak} | τ_{cen} |
|----------|--------|------------------------|------------------------|
| $H\beta$ | Year 2 | $8.52^{+2.23}_{-2.27}$ | $8.46^{+2.08}_{-2.14}$ |
| He II | Year 2 | $0.92^{+1.58}_{-2.42}$ | $0.84^{+2.05}_{-2.19}$ |
| Fe II | Year 2 | $3.51^{+1.49}_{-2.76}$ | $3.74^{+1.97}_{-2.62}$ |

To measure the line widths, we constructed mean and rms spectra following the equations below,

$$\langle f(\lambda) \rangle = \frac{1}{N} \sum_{i=1}^N f_i(\lambda), \quad (2)$$

$$\delta(\lambda) = \left[\frac{1}{N-1} \sum_{i=1}^N [f_i(\lambda) - \langle f(\lambda) \rangle]^2 \right]^{\frac{1}{2}}, \quad (3)$$

where $f_i(\lambda)$ is the flux of i th spectrum and N is the total number of spectra. For Year 1, we excluded the first five spectrum for constructing the mean and rms spectra. Due to the different instrumental set-up, those spectra can cause significant systemic uncertainty, particularly for the left wing of $H\beta$ line. In Figure 6, we present the mean and rms spectra of PG 0934+013, respectively for Year 1 and Year 2. In the upper panels, we first show the mean and rms spectra, which are made from individual spectra without subtracting power-law continuum and Fe II components. The rms spectrum reflects the variability of AGN continuum and Fe II components as the flux level is significantly larger than zero. In contrast, the rms spectrum in the bottom panel, which is made of individual spectra after subtracting power-law and Fe II components, shows much cleaner variability of the lines, e.g., $H\beta$ and He II. Note that [O III] is visible in the rms spectra, indicating that the flux rescaling was not perfect. Note that if we used the flux rescaled spectra based on the algorithm by Fausnaugh (2017), we also obtained a very similar rms spectrum.

To measure the line widths, we used the mean and rms spectra, which were constructed based on individual spectra after subtracting power-law and Fe II components. We measured both the full width at half-maximum (FWHM) and the second moment of each emission-line profile (i.e., line dispersion σ_{line} ; Peterson et al. 2004), which is defined as

$$\sigma_{\text{line}}^2 = \frac{\sum \lambda_i^2 f_i}{\sum f_i} - \lambda_0^2, \quad (4)$$

where f_i is the flux density and λ_i and λ_0 is the flux weighted centroid wavelength of the line profile. To measure line dispersion, we fitted the mean and rms spectra with a power-law model using the spectral regions which represents the continuum in the vicinity of the $H\beta$ line, in order to subtract the continuum. The uncertainty of line width measurements were determined by using the Monte Carlo bootstrap method (Peterson et al. 2004). From a set of N spectra, we randomly selected N spectra without considering previous selection. We then made mean and rms spectra for each realization to measure the line width. After constructing the distribution of line width measurements from 10,000 realizations, we adopted the standard deviation of the distribution as uncertainty. Note that the FWHM mea-

measurements using the rms spectra are relatively uncertain since the peak and the half-maximum are not straight forward to determine (Peterson et al. 2004). Thus, we provide FWHM and line dispersion measurements using the total $H\beta$ profile (without removing a narrow component) and the broad component of the line profile, respectively. Note that we constructed the rms and mean spectra, with/without removing the narrow component of $H\beta$ from individual single-epoch spectra, respectively, for measuring the width of the total $H\beta$ line profile or the broad component of $H\beta$ (see Table 5).

We present the line width measurements without spectral resolution correction in Table 5, to avoid any systematic uncertainty of the resolution in comparing line width measurements. For black hole mass calculation, we corrected for the spectral resolution ($R=1040$), which reduced the line width by only a few %.

In the case of the σ_{line} of $H\beta$, the measurements are similar regardless of the removing the narrow component of $H\beta$ since the second moment does not significantly depend on the peak of the line, while the σ_{line} measured from the mean spectra is significantly larger than that measured from the rms spectra. Similar discrepancy was reported in the previous studies (e.g., Bentz et al. 2006; Pei et al. 2014), suggesting that there may be a difference between the varying and non-varying parts of the BLR (for example, see the discussion in Park et al. 2012).

For black hole mass determination, the second moment of the $H\beta$ line in the rms spectrum is commonly used as the measure of line width because it is less sensitive to peaky line profiles. In this study we use the σ_{line} of $H\beta$, measured from the rms spectrum, which was constructed from individual spectra without removing the narrow component (bottom panels in Figure 6). Even if we remove the narrow component from $H\beta$ and construct the rms spectrum, the σ_{line} of $H\beta$ remains almost the same (see Table 5). In Table 6, we also present the line width measurements based on the mean and rms spectra, which are made of individual spectra after flux-rescaling using the code by Fausnaugh (2017). Based on this comparison we conclude that line width measurements are virtually the same regardless of the flux rescaling method.

We also measured the velocity and uncertainty of He II in the same manner (see Table 7). Since the narrow component in He II can be easily separated from the broad component in the He II line profile, we measured the FWHM and line dispersion from the broad component of He II, which were larger than those of $H\beta$ by a factor of two on average, indicating that He II emitting region is closer to the accretion disk than $H\beta$ emitting region as expected from the stratification (Wandel 1997; Peterson & Wandel 2000).

3.4. Black Hole Mass Determination

Assuming virial theorem, the mass of central black hole can be determined as

$$M_{\text{BH}} = f \frac{c\tau(\Delta V)^2}{G} \quad (5)$$

where f is a virial factor, which depends on the structure and kinematics of the BLR, ΔV is the width of broad emission line, τ is the time lag between continuum and emission line, c is the speed of light, and G is the

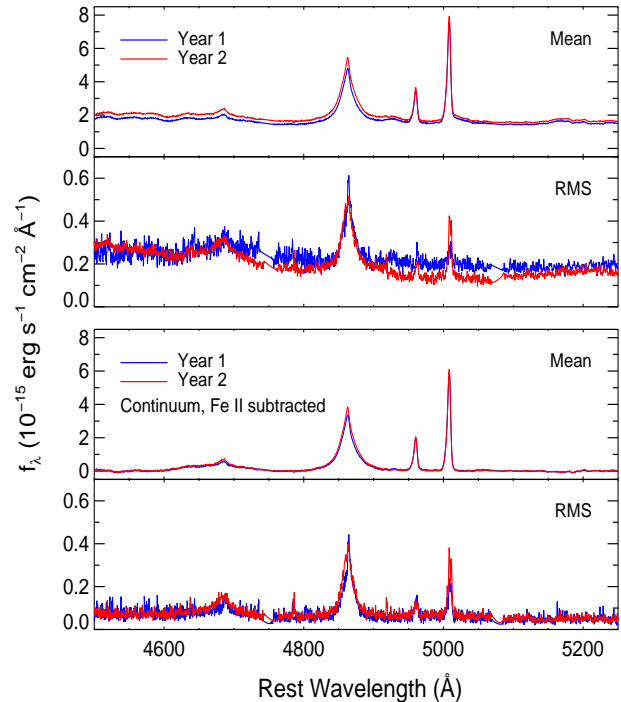


Figure 6. Mean and rms spectra of PG 0934+013, based on the individual spectra without removing power-law and Fe II components (top) and constructed from individual spectra after removing power-law and Fe II components (bottom), using Year 1 data (blue) or Year 2 data (red), respectively. All individual spectra are rescaled based on the [O III] line.

Table 5
Line width measurements from the total $H\beta$ line profile or the broad component of $H\beta$

| | | ΔV (BC+NC) | | ΔV (BC only) | |
|----------|------|-----------------------|------------------------|-----------------------|------------------------|
| | | FWHM | σ_{line} | FWHM | σ_{line} |
| | | (km s ⁻¹) | (km s ⁻¹) | (km s ⁻¹) | (km s ⁻¹) |
| Year 2 | mean | 1138 ± 14 | 1126 ± 10 | 1718 ± 23 | 1168 ± 16 |
| | rms | 930 ± 40 | 679 ± 45 | 1358 ± 49 | 641 ± 46 |
| Year 1+2 | mean | 1129 ± 13 | 1117 ± 8 | 1708 ± 20 | 1160 ± 12 |
| | rms | 1030 ± 45 | 660 ± 46 | 1449 ± 47 | 653 ± 46 |

Note. — The line widths (FWHM and σ_{line}) are measured from either mean or rms spectra, based on Year 2 data or the combined data of Year 1 and Year 2. Note that these measurements are presented without spectral resolution correction.

Table 6
Line width measurements from the total $H\beta$ line profile after flux-rescaling with the Fausnaugh (2017) algorithm.

| | | ΔV (BC+NC) | |
|----------|------|-----------------------|------------------------|
| | | FWHM | σ_{line} |
| | | (km s ⁻¹) | (km s ⁻¹) |
| Year 2 | mean | 1171 ± 15 | 1107 ± 9 |
| | rms | 959 ± 40 | 696 ± 46 |
| Year 1+2 | mean | 1143 ± 18 | 1121 ± 10 |
| | rms | 1011 ± 44 | 659 ± 45 |

Note. — The line widths (FWHM and σ_{line}) are measured from either mean or rms spectra, which are made of individual spectra after flux-rescaled with the code by Fausnaugh (2017). Note that these measurements are presented without spectral resolution correction.

Table 7
He II line width measurements

| Spectrum | | ΔV (BC only) | |
|----------|------|--------------------------------|--|
| | | FWHM (km s^{-1}) | σ_{line} (km s^{-1}) |
| Year 2 | mean | 5093 ± 31 | 2116 ± 23 |
| | rms | 2484 ± 53 | 1030 ± 47 |
| Year 1+2 | mean | 5683 ± 23 | 2031 ± 34 |
| | rms | 2487 ± 46 | 1045 ± 45 |

Note. — Note that these measurements are presented without spectral resolution correction.

Table 8
Black hole mass determination based on Year 2 data

| Spectrum | ΔV | M_{BH} (BC+NC) | M_{BH} (BC only) |
|----------|------------------------|------------------------------------|------------------------------------|
| | | (M_{\odot}) | (M_{\odot}) |
| Mean | FWHM | $2.13^{+0.55}_{-0.57} \times 10^6$ | $5.05^{+1.31}_{-1.35} \times 10^6$ |
| | σ_{line} | $8.80^{+2.28}_{-2.34} \times 10^6$ | $9.47^{+2.46}_{-2.53} \times 10^6$ |
| rms | FWHM | $1.38^{+0.38}_{-0.39} \times 10^6$ | $3.10^{+0.83}_{-0.85} \times 10^6$ |
| | σ_{line} | $3.13^{+0.91}_{-0.93} \times 10^6$ | $2.78^{+0.82}_{-0.84} \times 10^6$ |

gravitational constant. In order to determine M_{BH} , we employed the rest frame τ_{cen} of $\text{H}\beta$, after converting the measured time delay to the rest-frame time lag. We also used the line width of $\text{H}\beta$ (i.e., σ_{line} and FWHM, respectively) in the rms and mean spectra, which were generated from single-epoch spectra with/without removing the narrow component of $\text{H}\beta$ (see Table 5), after correcting for the spectral resolution. Here, we adopt the virial factor, $f = 4.47$ for the line dispersion of $\text{H}\beta$ and $f = 1.12$ for the FWHM of $\text{H}\beta$ based on the calibration by Woo et al. (2015). These virial factors were derived by normalizing the virial products to the $M_{\text{BH}} - \sigma_*$ relation of local galaxies with dynamical black hole mass measurements (e.g., Onken et al. 2004; Woo et al. 2010, 2015; Park et al. 2012; Grier et al. 2013). The uncertainties of M_{BH} were determined via error propagation from the uncertainty of the time lag and line width measurement.

The derived black hole mass ranges from $\sim 1.4 \times 10^6$ to $\sim 9.5 \times 10^6 M_{\odot}$ depending on the choice of the velocity measurements (see Table 8). As the best measurement, we combined σ_{line} measured from the total $\text{H}\beta$ line profile using the rms spectrum and the τ_{cen} measurement from Year 2 data, which provides $M_{\text{BH}} = 3.13^{+0.91}_{-0.93} \times 10^6 M_{\odot}$. On the other hand, if we use the FWHM measurement from the broad $\text{H}\beta$ component based on the rms spectrum, we obtained $M_{\text{BH}} = 3.10^{+0.83}_{-0.85} \times 10^6 M_{\odot}$. These two masses are consistent within the 1σ error. If the line width measurements from the mean spectrum are used, we obtain somewhat higher black hole masses due to the higher values of the line widths (see also Sergeev et al. 1999; Shapovalova et al. 2004; Collin et al. 2006; Park et al. 2012).

3.5. Velocity-resolved Lag

We investigate whether we can constrain the kinematic structure of the BLR by measuring the $\text{H}\beta$ velocity-resolved lags. After dividing the $\text{H}\beta$ line profile in the rms spectrum into several velocity channels, of which the velocity ranges were determined to have the same flux in each channel in the rms spectrum (see Fig. 7), we constructed a light curve for each velocity channel to cross-correlate it with the continuum light curve and obtained

the time lag and uncertainty for each velocity channel using the same Monte Carlo realizations as we used in S 3.2. We experimented with the number of the velocity channels, e.g., seven, five, and three, in order to reduce the uncertainty of the time lag measurements. However, the uncertainty of the time lags from each velocity channel is significantly larger than the difference of the time lags among velocity channels. As an example, we present the velocity resolved time lag measurements using three velocity channels, reporting that we obtained no meaningful trend due to the large error bars.

As a consistency check, we used the rms spectrum, which is made of individual single-epoch spectra after removing the narrow component of $\text{H}\beta$ (blue line in Figure 7), in order to investigate the effect of the narrow component. The rms spectrum without the narrow $\text{H}\beta$ component is less peaky than that with the narrow $\text{H}\beta$ component. We interpret that this is due to the uncertainty of removing the narrow component in each single-epoch spectrum. The narrow component can be subtracted somewhat more or somewhat less from each spectrum, and the fluctuation of this residual component from the narrow $\text{H}\beta$ compensates the variability of the broad $\text{H}\beta$ component. As we discussed in Section 3.2, this is why we used the spectra without removing the narrow $\text{H}\beta$ component for constructing the $\text{H}\beta$ light curve and measuring the time lag of $\text{H}\beta$. Nevertheless, we obtained consistent lag measurements within the error, regardless of removing the narrow $\text{H}\beta$ component.

4. DISCUSSION AND CONCLUSIONS

4.1. Mass determination

We performed photometric and spectroscopic monitoring observations over two sets of 4 month campaign to measure the emission line time lags and determine black hole mass of PG 0934+013. Based on the interpolation CCF analysis, we measured the centroid lag of $\text{H}\beta$ as $8.06^{+1.98}_{-2.04}$ days in the rest-frame based on Year 2 data, while the time lag from Year 1 data was not reliably determined. Using the total line profile of $\text{H}\beta$ in the rms spectrum, we obtained $\sigma_{\text{line}} = 668 \pm 44 \text{ km s}^{-1}$ after correcting for the spectral resolution. By applying the virial factor $f = 4.47$ from the recent calibration based on the $M_{\text{BH}} - \sigma_*$ relation by Woo et al. (2015), we determined $M_{\text{BH}} = 3.13^{+0.91}_{-0.93} \times 10^6 M_{\odot}$.

The M_{BH} of PG 0934+013 was previously estimated with single-epoch method in the literature. For example, Vestergaard & Peterson (2006) derived $M_{\text{BH}} = 7.041^{+0.092}_{-0.117} \times 10^7 M_{\odot}$, while Véron-Cetty et al. (2001) reported $M_{\text{BH}} = 4.3 \times 10^6 M_{\odot}$. If we use the SDSS spectrum of PG 0934+013, we derive $M_{\text{BH}} = 1.3 \times 10^7 M_{\odot}$ using $\text{FWHM}_{\text{H}\beta}$ and λL_{5100} . Note that the single epoch M_{BH} estimate varies due to a number of sources of systematic difference, i.e, a different virial factor (see Park et al. 2012), various methods of measuring the $\text{H}\beta$ line width, and the different calibration of the size-luminosity relation (see Bentz et al. 2013). Nevertheless, these single-epoch mass estimates are roughly consistent with our M_{BH} measurement based on the reverberation mapping result within a factor of several.

4.2. Size-luminosity relation

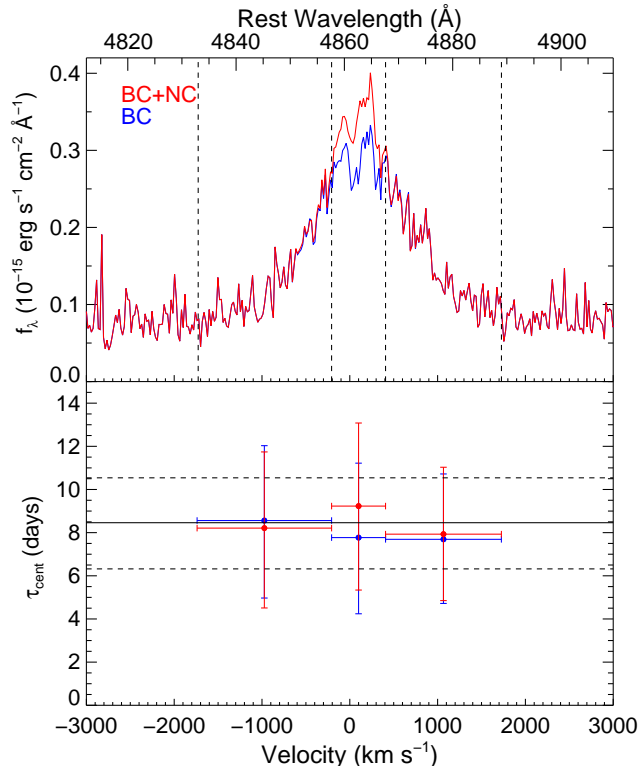


Figure 7. Velocity-resolved reverberation in the $H\beta$ line. The upper panel shows the $H\beta$ line profile in the rms spectrum without removing the narrow component (BC+NC; red line). In comparison we also present the rms spectrum made of individual spectra after removing the narrow $H\beta$ component (BC; blue line). Three velocity channels are denoted with dashed lines. The lower panel shows the time lag measured for each velocity channel with the horizontal error bar representing the width of the each velocity bin. The time lag based on the total line profile of $H\beta$ and its uncertainty are marked with solid and dashed lines, respectively.

We investigate whether the measured $H\beta$ lag is consistent with the size-luminosity relation. Using the measurement of $\lambda L_{5100} = 4.26 \times 10^{43} \text{ erg s}^{-1}$ from the mean spectrum of Year 2 data, we calculate the expected lag as $22.6^{+0.7}_{-0.7}$ days, based on the $H\beta$ lag-luminosity relation of Bentz et al. (2013). The expected lag is larger than our measurement of $8.46^{+2.08}_{-2.14}$ days by a factor of a few. Accounting for the uncertainty of the spectroscopic flux calibration, we re-measure the λL_{5100} after re-scaling the mean spectrum based on the photometry. Since the spectral range of our data does not cover the entire B band, we instead determine V band magnitude from the mean spectrum and converted it to B band magnitude with the measured color $B-V = 0.35$ from the SDSS spectrum of PG 0934+013, assuming that the color has not changed. In this process, we determine a scale factor of 0.9 based on the mean B band magnitude of 16.40 ± 0.07 from our photometric campaign in Year 2. If we use the scaled λL_{5100} , then the expected lag becomes $21.85^{+0.68}_{-0.67}$ days.

In Figure 8 we present the size-luminosity relation of the reverberation-mapped AGNs from Bentz et al. (2013) along with our measurements of PG 0934+013. We point out that the λL_{5100} measurement is relatively uncertain. The source of uncertainty of the λL_{5100} includes the spectroscopic flux calibration and the rescal-

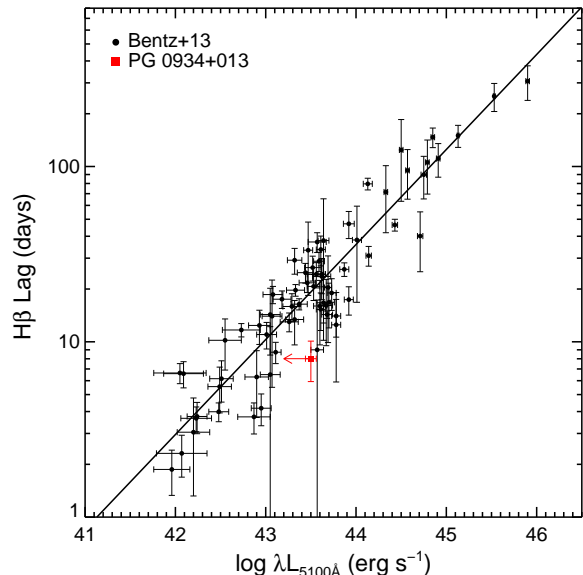


Figure 8. Size-luminosity relation adopted from Bentz et al. (2013) along with our measurements of PG 0934+013 (red square). We adopted the AGN luminosity estimated based on the HST WFC3 F438W image. Since the host galaxy contribution is relatively uncertain, we denoted the luminosity with an upper limit sign.

ing of the flux based on photometry, and the variability of the source during the campaign. The rms variability of the source during the campaign is larger than the typical measurement error of the flux at 5100Å in each spectrum. Note that if the host galaxy stellar continuum is not subtracted from the observed flux, the measured λL_{5100} can be considered as an upper limit. For luminous AGNs, stellar contribution to λL_{5100} is negligible. However, it is necessary to correct for the host galaxy contribution for moderate to low luminosity AGNs such as PG 0934+013 (e.g., Bentz et al. 2013). Although we included a stellar population model in the spectral decomposition process for several epochs as these spectra with a high S/N ratio showed stellar absorption features, we were not able to reliably quantify stellar fraction in the monochromatic luminosity at 5100Å based on these spectra.

Deep high resolution imaging data are required to provide a robust measurement of λL_{5100} from AGN component, via, for example, the 2-D surface bright fitting analysis. The available HST WFC3 archival images of PG 0934+013 are relatively shallow with a 450 second exposure in the F438W band and a 300 second exposure in the F814W band, which are not sufficient to obtain rigorous results with the AGN-galaxy decomposition analysis based on our experience (Bennert et al. 2010; Park et al. 2015). Nevertheless, we tried to use both F438W and F814W band images of PG 0934+013 to estimate the AGN fraction. Since a stellar bar is clearly present in the raw image, we used two components for the host galaxy, namely, a bulge (Sersic index $n=4$) and a bar ($n=0.5$), along with a PSF component, which was constructed with the TinyTim, for a 2-D surface brightness fitting with the GALFIT (Peng et al. 2002). Although it is difficult to constrain the host galaxy structure, we were able to obtain a reasonable fit with the three components al-

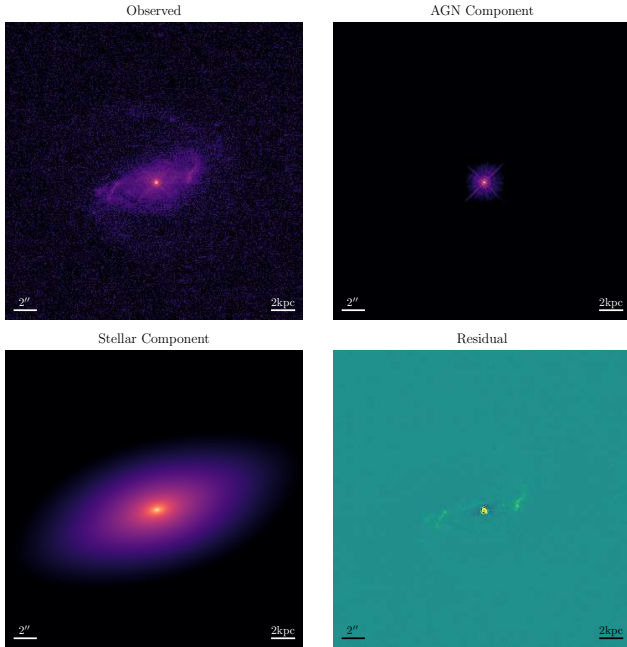


Figure 9. 2-D decomposition of PG 0934+013 (upper left), using a PSF for AGN (upper right) and two components (bulge and bar) for the host galaxy (lower left) based on the F438W band image obtained with the HST WCF3.

beit with a large residual, particularly at the spiral structure, and measured the fraction of the PSF component as presented in Figure 9. The AGN fraction is 0.38 in the total flux observed through the F438W band. In the case of the F814W band image, the AGN fraction is 0.42. If we apply the same aperture used for spectroscopy, this fraction increases to 0.71 and 0.61, respectively for F438W and F814W images since the host galaxy flux is more widely distributed than the point source. On the other hand, if we convolve with a typical ground-based seeing, the AGN fraction may also change depending on the exact radial profile of the host galaxy. We experimented with a series of seeing size to degrade the HST image to investigate the seeing effect. We find that the AGN fraction changes insignificantly within a several % level. Although the AGN fraction is wavelength-dependent, if we take the face value of the AGN fraction (i.e., 0.42) based on the F814W band image in order to correct for the host galaxy contribution, then the AGN continuum luminosity becomes $\lambda L_{5100} = 1.61 \times 10^{43} \text{ erg s}^{-1}$, and the expected lag from the size-luminosity relation is ~ 13 days. Based on the F438W band magnitude of the AGN from the decomposition analysis, we determine the continuum luminosity at 5100\AA , using the SDSS spectra after rescaling the flux to match the F438W band magnitude. The obtained luminosity is $\lambda L_{5100} = 3.14 \times 10^{43} \text{ erg s}^{-1}$, as shown in Figure 8. Considering the flux uncertainties and systematic effects, i.e., host galaxy contribution, we find no strong evidence that PG 0934+013 deviates from the size-luminosity relation. A more detailed analysis on the host galaxy based on a high quality imaging data is necessary to confirm whether PG 0934+013 follows the size-luminosity relation.

Recent reverberation studies on narrow-line Seyfert 1 galaxies claimed that super-Eddington AGNs have shorter $H\beta$ lags than the expected lag from the size-

luminosity relation (Du et al. 2015, 2016). However, since the Eddington ratio of PG 0934+013 is $\sim 1\%$, which is calculated using the observed luminosity at 5100\AA (λL_{5100}) without considering host galaxy contribution after multiplying a bolometric correction factor 10 (Woo & Urry 2002), it is not relevant to compare the target with the high Eddington AGNs in the context of the size-luminosity relation.

4.3. $M_{\text{BH}} - \sigma_*$ relation

Finally, we discuss whether PG 0934+013 follows the scaling relations between M_{BH} and galaxy properties. Since the stellar velocity dispersion of PG 0934+013 has not been reported in the literature, we tried to measure it using our own spectrum obtained with the best sky condition although the stellar continuum is still very noisy. After masking out the emission line $[\text{N I}] \lambda 5201$, we obtained $\sigma_* = 77 \pm 34 \text{ km s}^{-1}$ from the stellar absorption lines in the spectral range $5150\text{--}5300 \text{ \AA}$, using the penalized pixel-fitting (pPXF) method and the MILES stellar population models with a solar metallicity (Cappellari & Emsellem 2004). In Figure 10, we present the M_{BH} -stellar velocity dispersion relation defined with a joint-analysis of inactive and active galaxies from Woo et al. (2015, see also Woo et al. (2013)), along with our measurements of PG 0934+013. While the stellar velocity dispersion measurement is highly uncertain due to the low S/N on stellar continuum and relatively low spectral resolution (i.e., line dispersion resolution $\sigma = 122 \text{ km s}^{-1}$), we find no significant evidence that whether PG 0934+013 offsets from the $M_{\text{BH}} - \sigma_*$ relation defined by inactive galaxies and other reverberation-mapped AGNs (Woo et al. 2013, 2015). Further investigations with much better data and measurement is necessary to investigate the case.

Our reverberation study demonstrates that large telescopes equipped with a queue observation mode can be effectively used for time series studies of AGNs. The capability of the SALT for regular access and sensitivity will be very useful for future reverberation studies of both low luminosity AGNs, which requires a short cadence, and for high- z AGNs, which requires a large photon-collecting power.

We thank the anonymous referee for various suggestions, which were helpful to improve the clarity of the paper. This work was supported by Samsung Science and Technology Foundation under Project Number SSTF -BA1501-05 and the National Research Foundation of Korea grant funded by the Korea government (No. 2016R1A2B3011457). E.R.C. and S.C. gratefully acknowledge the receipt of research grants from the National Research Foundation (NRF) of South Africa. C.C. and M.I. acknowledges the support from National Research Foundation of Korea grant, No. 2008-0060544, funded by the Korean government (MSIP). This work is partially based on the data collected from the Mt. Lemmon Optical Astronomy Observatory operated by Korea Astronomy and Space Science Institute. Spectroscopic observations reported in this paper were obtained with

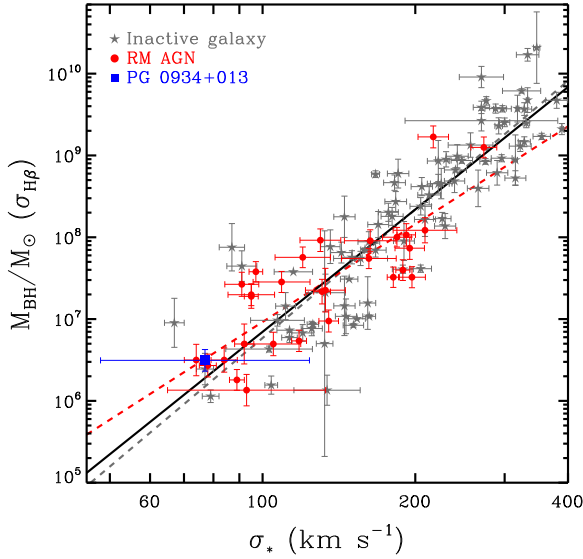


Figure 10. $M_{\text{BH}} - \sigma_*$ relation of reverberation-mapped AGNs (red filled circles) and inactive galaxies (grey stars) adopted from Woo et al. (2015), including our measurement of PG 0934+013 (blue square). The solid line is the best fit from Woo et al. (2015), while the dashed lines represent the best fit respectively for reverberation-mapped AGNs (red) and inactive galaxies.

the Southern African Large Telescope (SALT).

REFERENCES

- Bennert, V. N., Treu, T., Auger, M. W., et al. 2015, *ApJ*, 809, 20
 Blandford, R. D., & McKee, C. F. 1982, *ApJ*, 255, 419
 Barth, A. J., Ho, L. C., & Sargent, W. L. W. 2002, *ApJ*, 566, L13
 —. 2003, *ApJ*, 583, 134
 Barth, A. J., Pancoast, A., Thorman, S. J., et al. 2011, *ApJ*, 743, L4
 Barth, A. J., Pancoast, A., Bennert, V. N., et al. 2013, *ApJ*, 769, 128
 Barth, A. J., Bennert, V. N., Canalizo, G., et al. 2015, *ApJS*, 217, 26
 Bentz, M. C., Denney, K. D., Cackett, E. M., et al. 2006, *ApJ*, 651, 775
 Bennert, V. N., Treu, T., Woo, J.-H., et al. 2010, *ApJ*, 708, 1507
 Bennert, V. N., Auger, M. W., Treu, T., Woo, J.-H., & Malkan, M. A. 2011, *ApJ*, 742, 107
 Bentz, M. C., Peterson, B. M., Netzer, H., Pogge, R. W., & Vestergaard, M. 2009a, *ApJ*, 697, 160
 —. 2009b, *ApJ*, 697, 160
 Bentz, M. C., Walsh, J. L., Barth, A. J., et al. 2010, *ApJ*, 716, 993
 Bentz, M. C., Denney, K. D., Grier, C. J., et al. 2013, *ApJ*, 767, 149
 Boroson, T. A. 2002, *ApJ*, 565, 78
 Boroson, T. A., & Green, R. F. 1992, *ApJS*, 80, 109
 Bower, R. G., Benson, A. J., Malbon, R., et al. 2006, *MNRAS*, 370, 645
 Brewer, B. J., et al. 2011, *ApJ*, 733, L33
 Buckley, D. A. H., Swart, G. P., & Meiring, J. G. 2006, *Proc. SPIE*, 6267, 62670Z
 Burgh, E. B., Nordsieck, K. H., Koblunicky, H. A., et al. 2003, *Proc. SPIE*, 4841, 1463
 Cappellari, M., & Emsellem, E. 2004, *PASP*, 116, 138
 Cisternas, M., Jahnke, K., Inskip, K. J., et al. 2011, *ApJ*, 726, 57
 Collin, S., Kawaguchi, T., Peterson, B. M., & Vestergaard, M. 2006, *A&A*, 456, 75
 Crawford, S. M., Still, M., Schellart, P., et al. 2010, *Proc. SPIE*, 7737, 773725
 Davis, S. W., Woo, J.-H., & Blaes, O. M. 2007, *ApJ*, 668, 682
 Denney, K. D., Bentz, M. C., Peterson, B. M., et al. 2006, *ApJ*, 653, 152
 Denney, K. D., Peterson, B. M., Pogge, R. W., et al. 2010, *ApJ*, 721, 715
 Du, P., Lu, K.-X., Zhang, Z.-X., et al. 2016, *ApJ*, 825, 126
 Du, P., Hu, C., Lu, K.-X., et al. 2015, *ApJ*, 806, 22
 Peterson, B. M., Grier, C. J., et al. 2012, *ApJ*, 757, 53
 Edelson, R., Turner, T. J., Pounds, K., et al. 2002, *ApJ*, 568, 610
 Fausnaugh, M. M., Grier, C. J., Bentz, M. C., et al. 2017, *ApJ*, 840, 97
 Fausnaugh, M. M. 2017, *PASP*, 129, 024007
 Ferrarese, L., & Merritt, D. 2000, *ApJ*, 539, L9
 Ferrarese, L., Pogge, R. W., Peterson, B. M., et al. 2001, *ApJ*, 555, L79
 Gaskell, C. M., & Peterson, B. M. 1987, *ApJS*, 65, 1
 Gebhardt, K., Bender, R., Bower, G., et al. 2000, *ApJ*, 539, L13
 Goodrich, R. W. 1989, *ApJ*, 342, 224
 Grupe, D. 2004, *AJ*, 127, 1799
 Grier, C. J., Martini, P., Watson, L. C., et al. 2013, *ApJ*, 773, 90
 Grupe, D., & Mathur, S. 2004, *ApJ*, 606, L41
 Jahnke, K., Bongiorno, A., Brusa, M., et al. 2009, *ApJ*, 706, L215
 Häring, N., & Rix, H.-W. 2004, *ApJ*, 604, L89
 Horne, K., Peterson, B. M., Collier, S. J., & Netzer, H. 2004, *PASP*, 116, 465
 Hu, C., Du, P., Lu, K.-X., et al. 2015, *ApJ*, 804, 138
 Kaspi, S., Maoz, D., Netzer, H., et al. 2005, *ApJ*, 629, 61
 Kaspi, S., Smith, P. S., Netzer, H., et al. 2000, *ApJ*, 533, 631
 Koblunicky, H. A., Nordsieck, K. H., Burgh, E. B., et al. 2003, *Proc. SPIE*, 4841, 1634
 Kollmeier, J. A., Onken, C. A., Kochanek, C. S., et al. 2006, *ApJ*, 648, 128
 Kormendy, J., & Ho, L. C. 2013, *ARA&A*, 51, 511
 Kovačević, J., Popović, L. C., & Dimitrijević, M. S. 2010, *ApJS*, 189, 15
 Kollatschny, W. 2003, *A&A*, 407, 461
 Krongold, Y., Dultzin-Hacyan, D., & Marziani, P. 2001, *AJ*, 121, 702
 Lawrence, A., Saunders, W., Rowan-Robinson, M., et al. 1988, *MNRAS*, 235, 261
 Markwardt, C. B. 2009, in *Astronomical Society of the Pacific Conference Series*, Vol. 411, *Astronomical Data Analysis Software and Systems XVIII*, ed. D. A. Bohlender, D. Durand, & P. Dowler, 251
 McConnell, N. J., & Ma, C.-P. 2013, *ApJ*, 764, 184
 McGill, K. L., Woo, J.-H., Treu, T., & Malkan, M. A. 2008, *ApJ*, 673, 703-714
 Merloni, A., Bongiorno, A., Bolzonella, M., et al. 2010, *ApJ*, 708, 137
 Merritt, D., & Ferrarese, L. 2001, *ApJ*, 547, 140
 Nelson, C. H., & Whittle, M. 1995, *ApJS*, 99, 67
 Netzer, H., Maoz, D., Laor, A., et al. 1990, *ApJ*, 353, 108
 Onken, C. A., Ferrarese, L., Merritt, D., et al. 2004, *ApJ*, 615, 645
 Osterbrock, D. E. 1978, *Proceedings of the National Academy of Science*, 75, 540
 Osterbrock, D. E., & Pogge, R. W. 1985, *ApJ*, 297, 166
 Park, D., Woo, J.-H., Treu, T., et al. 2012, *ApJ*, 747, 30
 Park, D., Woo, J.-H., Treu, T., et al. 2012, *ApJ*, 747, 30
 Park, D., Woo, J.-H., Bennert, V. N., et al. 2015, *ApJ*, 799, 164
 Park, D., Barth, A. J., Woo, J.-H., et al. 2017, *ApJ*, 839, 93
 Pancoast, A., Brewer, B. J., Treu, T., et al. 2012, *ApJ*, 754, 49
 Peng, C. Y., Ho, L. C., Impey, C. D., & Rix, H.-W. 2002, *AJ*, 124, 266
 Peng, C. Y., Impey, C. D., Rix, H.-W., et al. 2006, *ApJ*, 649, 616
 Pei, L., Barth, A. J., Aldering, G. S., et al. 2014, *ApJ*, 795, 38
 Peterson, B. M. 1993, *PASP*, 105, 247
 Peterson, B. M., & Ferland, G. J. 1986, *Nature*, 324, 345
 Peterson, B. M., & Wandel, A. 2000, *ApJ*, 540, L13
 Peterson, B. M., Ferrarese, L., Gilbert, K. M., et al. 2004, *ApJ*, 613, 682
 Peterson, B. M., Ferrarese, L., Gilbert, K. M., et al. 2004, *ApJ*, 613, 682
 Rafter, S. E., Kaspi, S., Behar, E., Kollatschny, W., & Zetzl, M. 2011, *ApJ*, 741, 66
 Rodríguez-Pascual, P. M., Alloin, D., Clavel, J., et al. 1997, *ApJS*, 110, 9
 Sergeev, S. G., Pronik, V. I., Sergeeva, E. A., & Malkov, Y. F. 1999, *AJ*, 118, 2658
 Shapovalova, A. I., Doroshenko, V. T., Bochkarev, N. G., et al. 2004, *A&A*, 422, 925
 Shen, Y., Horne, K., Grier, C. J., et al. 2015, *arXiv:1510.02802*
 Schmidt, M., & Green, R. F. 1983, *ApJ*, 269, 352
 Tremaine, S., Gebhardt, K., Bender, R., et al. 2002, *ApJ*, 574, 740

- Treu, T., Woo, J.-H., Malkan, M. A., & Blandford, R. D. 2007, *ApJ*, 667, 117
- Valenti, S., Sand, D. J., Barth, A. J., et al. 2015, *ApJ*, 813, L36
- van der Marel, R. P. 1994, *MNRAS*, 270, 271
- van Dokkum, P. G. 2001, *PASP*, 113, 1420
- van Groningen, E., & Wanders, I. 1992, *PASP*, 104, 700
- Véron-Cetty, M.-P., Véron, P., & Gonçalves, A. C. 2001, *A&A*, 372, 730
- Vestergaard, M., & Peterson, B. M. 2006, *ApJ*, 641, 689
- Wandel, A. 1997, *ApJ*, 490, L131
- Wandel, A., Peterson, B. M., & Malkan, M. A. 1999, *ApJ*, 526, 579
- White, R. J., & Peterson, B. M. 1994, *PASP*, 106, 879
- Woo, J.-H., & Urry, C. M. 2002, *ApJ*, 579, 530
- Woo, J.-H., Treu, T., Malkan, M. A., & Blandford, R. D. 2006, *ApJ*, 645, 900
- Woo, J.-H., Treu, T., Malkan, M. A., & Blandford, R. D. 2008, *ApJ*, 681, 925
- Woo, J.-H., Treu, T., Barth, A. J., et al. 2010, *ApJ*, 716, 269
- Woo, J.-H., Schulze, A., Park, D., et al. 2013, *ApJ*, 772, 49
- Woo, J.-H., Yoon, Y., Park, S., Park, D., & Kim, S. C. 2015, *ApJ*, 801, 38
- Woo, J.-H., Bae, H.-J., Son, D., & Karouzos, M. 2016, *ApJ*, 817, 108